

Optimization of A Mobile Optical SWIPT System With Asymmetric Spatially Separated Laser Resonator

Mingliang Xiong, Qingwen Liu, *Senior Member, IEEE*, and Shengli Zhou *Fellow, IEEE*

Abstract—High-power and high-rate simultaneous wireless information and power transfer (SWIPT) becomes more and more important with the development of Internet of Things technologies. Optical SWIPT, also known as simultaneous light information and power transfer (SLIPT), has unique advantages such as abundant spectrum resources and low propagation divergence, compared with radio-frequency (RF) SWIPT. However, optical SWIPT faces many challenges in beam steering and receiver positioning/tracking. Resonant beams generated by spatially separated laser resonators (SSLR) have many advantages, including high power, self-aligned mobility, and intrinsic safety. It has been proposed as the carrier of wireless charging and communication. Using resonant beams, mobile electronic devices can be remotely charged and supported with high-rate data transfer. In this paper, we propose a mobile optical SWIPT system based on asymmetric SSLR and present the system optimization procedure. We also determine the boundary of the charging power and communication rate, and discuss the trade-off between power transfer and information transfer. Numerical results show that both the charging power and the communication rate of the optimized asymmetric system are much higher than those of the symmetric system in the previous work.

Index Terms—Resonant beam communications, resonant beam charging, distributed laser charging, laser communications, wireless power transfer, 6G mobile network.

I. INTRODUCTION

WITH the development of the Internet of Things, high-power and high-rate simultaneous wireless information and power transfer (SWIPT) becomes more and more important. For example, augmented reality and virtual reality headsets need more energy than common mobile devices for high performance computing, and at the same time need high communication rate to exchange the three-dimensional (3D) holographic information [1]. Another example is the unmanned aerial vehicle (UAV) which becomes popular in digital city and some other scenarios [2]. UAVs require high-speed channel to transfer high-definition (HD) videos, and simultaneously need enough power to expand the flying time as long as possible. Especially in the six generation (6G) mobile networks, charging a mobile device via radio wave or

The corresponding author: Qingwen Liu.

This work was supported in part by the National Natural Science Foundation of China under Grant 62071334, in part by the National Key Research and Development Project under Grant 2020YFB2103900 and Grant 2020YFB2103902, in part by the Shanghai Municipal Science and Technology Major Project under Grant 2021SHZDZX0100, and in part by the Shanghai Municipal Commission of Science and Technology Project under Grant 19511132101.

M. Xiong and Q. Liu are with the College of Electronics and Information Engineering, Tongji University, Shanghai 201804, China (e-mail: xionglm@tongji.edu.cn; qliu@tongji.edu.cn). S. Zhou is with Department of Electrical and Computer Engineering, University of Connecticut, Storrs, CT 06250, USA (e-mail: shengli.zhou@uconn.edu).

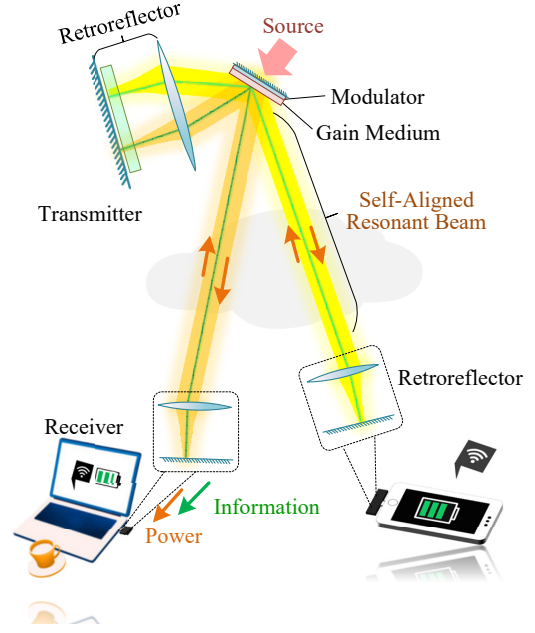


Fig. 1. Scenario and mechanism of mobile optical SWIPT using self-aligned resonant beam

laser beam is an anticipated innovation to enable many new applications [3].

Optical SWIPT exhibits distinctive advantages which can complement the weakness of radio frequency (RF) technologies, especially in indoor environments [4]. Light wave has extremely high frequency, which provides a broad communication band. Besides, since light has much shorter wavelength than RF, its power can be compressed in a narrow beam (e.g., laser usually has millimeter-level beam radius) to reduce the path loss. The beam width in RF beamforming is proportional to the wavelength and inversely proportional to the number of antenna elements and the element separation [5]. As the element separation should be greater than half of the wavelength, it brings a limitation to the element number with a given antenna area and thus prompts the requirement of shortening the wavelength. Motivated by this, simultaneous light information and power transfer (SLIPT) is receiving more and more attention [6].

Nevertheless, optical SWIPT still faces many challenges. For instance, the received power and the coverage area are two conflicting aspects. Visible light communications (VLC) technologies aim to cover the whole room by emitting the light wave to everywhere [7]. In this case, the optical power received by the receiver is very low, as most power is wasted in the

space. On the other hand, although the light can be focused on the receiver to improve the received power as high as possible, it faces challenges in beam steering and receiver positioning/tracking, especially for long-range applications [8]. Many works paid attention to the response speed of beam steering. For instance, in-fiber diffraction gratings employed for beam steering exhibit faster response than micro-electromechanical systems (MEMS) [9]. Two-dimensional (2D) fiber arrays [10], crossed gratings [11], and silicon optical phased arrays (OPA) are also good technologies for fast beam steering [12]. Besides, beam steering with spatial light modulator (SLM) is an effective way to realize point-to-multipoint mobile optical communications (MOC) [13]. However, the angle resolution of beam steering limits the acceptable distance of targets. The alignment and tracking also rely on the accuracy and the processing speed of existing positioning technologies [14].

Resonant beam has been proposed as the carrier of wireless charging and communication for its advantages including high power, self-aligned mobility, and intrinsic safety [15, 16]. As shown in Fig. 1, the resonant beam is generated by a spatially separated laser resonator (SSLR) which consists of two retroreflectors – one at the transmitter and the other at the receiver. The retroreflectors can be corner cubes, cat’s eyes, or telecentric cat’s eyes. They have the ability to reflect the incident lights back to the source. Lights can oscillate between two retroreflectors with many round trips. If a gain medium is placed inside the resonator, the oscillating lights will be amplified, and then, form an intra-cavity resonant beam.

The primary idea of using two corner cubes to create a very long laser (up to 30 km) was proposed in [17]. Resonant beam communications (RBCom) based on telecentric cat’s eye retroreflector (TCR) is proposed in [18]. Paper [18] also proposed a focal TCR (FTCR) design and demonstrated that resonators based on FTCRs can reach a stable regime where the intra-cavity diffraction loss is extremely low. The light-field simulation of the SSLR was conducted to verify its mobility [19]. The safety of the resonant beam has also been analyzed through light-field simulation [20]. An experiment on charging a smart phone via the resonant beam generated from the FTCR-based SSLR was demonstrated in [21], which achieved above 5-W received optical power and 0.6-W battery charging power within 2-m distance, and also with a maximum horizontal moving range of ± 18 cm. Besides, Wang *et al.* also conducted experiments on the TCR-based SSLR and demonstrated the adjustable-free range of $\pm 13^\circ$ [22]. Lim *et al.* proposed and did experiments on a new SSLR cavity based on spatial wavelength division and diffraction gratings, which realized 1.7-mW received power at 1-m distance [23]. Liu *et al.* expanded the field of view (FOV) of the SSLR receiver to $\pm 30^\circ$ over 5-m working distance in experiment [24]. Capacity of the RBCom system based on corner cubes was analyzed in [25]. To overcome the intra-cavity echo interference, an intra-cavity second harmonic generation (SHG) scheme was adopted in the RBCom system [26].

Mobile optical SWIPT based on symmetric SSLR and intra-cavity SHG was proposed in [27]. However, the symmetric SSLR exhibits relatively low energy efficiency, as the beam waist locates at the midpoint of the resonator rather than

the location of the gain medium. Only with an asymmetric SSLR, can the beam waist be moved to the position of the gain medium. But, an asymmetric SSLR is really different from what we have studied in the previous work, as many parameters need to be determined. How can we create an asymmetric SSLR with proper parameters for better SWIPT performance than the previous design in [27]? – This question motivated this research.

The contributions of this work are as follows.

- 1) We propose the asymmetric SSLR-based mobile optical SWIPT system to provide a performance improvement compared with the symmetric system in the previous work. In the asymmetric SSLR, the two retro-reflectors have different parameters, so that the intra-cavity beam waist can be much closer to the gain medium than the symmetric SSLR whose beam waist is assured locating at the midpoint of the resonator, which improves the energy conversion efficiency of the gain medium.
- 2) Since the asymmetric SSLR has several undetermined parameters, we present a procedure to obtain the optimum parameters for the system. Using the optimization procedure, we determine the region and the boundary of the achievable charging power and achievable rate. We also discuss the trade-off between power transfer and information transfer.

The remainder of this paper is organized as follows. In Section II, we propose the system model of the asymmetric SSLR-based mobile optical SWIPT system. All the theory are presented in this Section II. Then, we use two separated sections, Section III and Section IV, to present the optimization and the trade-off procedures, respectively, as they have different purposes and should be conducted in order. Specifically, in Section IV we demonstrate the performance boundary and discuss the trade-off on charging power and communication rate. The performance improvement is also verified in Section IV. At last, we conclude in Section V.

II. SYSTEM MODEL

The mobile optical SWIPT system is based on the asymmetric SSLR structure and the intra-cavity SHG scheme. The resonant beam generated by the SSLR is employed as the power transfer carrier; and simultaneously, a small portion of the resonant beam is converted into a frequency-doubled SHG beam for information transfer. For better understanding of this work, we first describe the basic structure of the SSLR and the intra-cavity SHG scheme, although the detailed information can be found in the previous work [27]. Then, we present the system model of the asymmetric structure and point out the parameters that can be optimized.

The mobile ability of this SWIPT system is supported by the SSLR, specifically by the retroreflectors in the SSLR. As is known, a typical laser cavity is comprised of two spherical mirrors that are set parallel to each other. According to the theory of resonator presented in [28], photons captured by a stable cavity will oscillate many times between two mirrors. The loss of photons is compensated for by the amplification of the gain medium between the mirrors. Similarly, the SSLR

pump light which is generated by a laser diode module driven with input electrical power P_{in} to obtain the optical amplification ability. The photons are consumed during oscillation and compensated by the stimulated emission occurring in the gain medium, which reaches a balance as time goes on. At the receiver, a portion of the oscillating photons are allowed to pass through the output mirror M2, and the other part is reflected back to maintain the resonance. A photovoltaic panel (PV) converts these output photons into electricity to charge the battery. To realize SWIPT, the information is modulated on the frequency-doubled SHG beam (at the second-harmonic frequency 2ν). The SHG beam is generated from the resonant beam by the SHG medium placed inside the resonator. This is practical as the intra-cavity SHG has been well studied [32–34]. The light intensity of the SHG beam is modulated by the electro-optic modulator (EOM) placed near the gain medium. Due to the frequency difference from the resonant beam, the SHG beam can be totally allowed to pass through M2 and bring information to the photon detector (PD). As we propose a SWIPT scheme, the receiver should have the ability of splitting the information and the power. Generally, there are many splitting methods for RF-based SWIPT, such as time switching, power splitting, receiver separation, and antenna switching [35]. However, in this paper, based on the wide-spectrum advantage of light, we transfer power and information by different light frequencies and use dichroic mirror M3 to extract the SHG beam from the mixed beam by frequency difference. This can be realized provided that M2 and M3 are coated with partially-reflective (PR), anti-reflective (AR), or high-reflective (HR) coatings at corresponding frequencies (ν or 2ν). Since the beams for information transfer and power transfer are with separated paths in the receiver, we use lens L3 to focus the power transfer beam on the PV and use lens L4 to focus the information transfer beam on the PD.

The asymmetric SSLR is comprised of two different FTCRs RR1 and RR2. At the transmitter, the focal length of the lens L1 is f_1 , and the space interval between L1 and the mirror M1 is l_1 . While at the receiver, the focal length and the lens-to-mirror interval with respect to RR2 are f_2 and l_2 , respectively. We term the outer focal plane of an FTCR as its input/output (IO) plane, and take the space interval between the IO planes of the two FTCRs in the SSLR as the transmission distance d . An optical resonator can be expressed by its signal-pass ray-transfer matrix [36, 37]. We can use this matrix to analyze the resonator's characteristic, including the stability and the distribution of the intra-cavity beam radius (cf. Chapter 8 in [28]). Then, the single-pass ray-transfer matrix of the asymmetric SSLR yields [18]

$$\begin{bmatrix} A & B \\ C & D \end{bmatrix} = \begin{bmatrix} 1 & 0 \\ 0 & 1 \end{bmatrix} \begin{bmatrix} 1 & l_2 \\ 0 & 1 \end{bmatrix} \begin{bmatrix} 1 & 0 \\ -1/f_2 & 1 \end{bmatrix} \begin{bmatrix} 1 & f_1 + f_2 + d \\ 0 & 1 \end{bmatrix} \\ \begin{bmatrix} 1 & 0 \\ -1/f_1 & 1 \end{bmatrix} \begin{bmatrix} 1 & l_1 \\ 0 & 1 \end{bmatrix} \begin{bmatrix} 1 & 0 \\ 0 & 1 \end{bmatrix}. \quad (5)$$

By calculating the ABCD matrix expressed by (5), we obtain

the elements in the matrix as follows:

$$\begin{cases} A = -\frac{f_2}{f_1} - \frac{d}{f_1} + \frac{dl_2}{f_1 f_2}, \\ B = f_1 + f_2 - \frac{l_2(f_1 + d)}{f_2} - \frac{l_1(f_2 + d)}{f_1} + \frac{dl_1 l_2}{f_1 f_2} + d, \\ C = \frac{d}{f_1 f_2}, \\ D = -\frac{f_1}{f_2} - \frac{d}{f_2} + \frac{dl_1}{f_1 f_2}. \end{cases} \quad (6)$$

A stable resonator means that rays oscillating in this resonator can not escape, and therefore, the diffraction loss is extremely low. The ABCD elements in (6) can be utilized to judge SSLR's stability and calculate the beam radius distribution along the optical axis by adopting the method of creating an equivalent resonator which has two g -parameters g_1^* and g_2^* , and a cavity length L^* [28, 36, 37]. Let $g_1^* = A$, $g_2^* = D$, we calculate the resonator's stability with the following quantity:

$$g_1^* g_2^* = \frac{(f_1^2 + df_1 - dl_1)(f_2^2 + df_2 - dl_2)}{f_1^2 f_2^2}. \quad (7)$$

For a stable resonator, the following stable condition should be met [28]:

$$0 < g_1^* g_2^* < 1. \quad (8)$$

Generally, there are multiple transverse modes in a laser resonator. All these existing modes add up to form the laser beam. Among these modes, the fundamental mode TEM_{00} exhibits the smallest radius. The TEM_{00} mode radius at location z on the optical axis is obtained by [28]

$$w_{00}(z) = \sqrt{-\frac{\lambda}{\pi \Im[1/q(z)]}}, \quad (9)$$

where $\lambda = c/\nu$ is the wavelength, c is the light speed, and $\Im[\cdot]$ takes the imaginary part of a complex number. Here, parameter $q(z)$ records all the information of the TEM_{00} mode, such as the mode radius, the radius of curvature of the constant phase surface, and the divergence angle. Let $L^* = B$, we can compute all the $q(z)$ parameters of an FTCR-based asymmetric SSLR as [18]

$$q(z) = \begin{cases} j|L^*| \sqrt{\frac{g_2^*}{g_1^*(1-g_1^*g_2^*)}} + z, & z \in [0, z_{L1}], \\ \frac{q(z_{L1})}{-q(z_{L1})/f_1 + 1} + (z - z_{L1}), & z \in (z_{L1}, z_{L2}], \\ \frac{q(z_{L2})}{-q(z_{L2})/f_2 + 1} + (z - z_{L2}), & z \in (z_{L2}, z_{M2}], \end{cases} \quad (10)$$

where $j = \sqrt{-1}$; and z_{L1} , z_{L2} , and z_{M2} represent the location of L1, L2, and M2, respectively.

The resonant beam radius is proportional to its TEM_{00} mode radius. This proportion is called the beam propagation factor; and it is a constant at any location on the optical axis. Assuming the gain medium has the smallest aperture among all the devices in the resonator and most diffraction loss comes

from the gain medium aperture, we can approximate the beam radius at location z by [28]

$$w(z) = \frac{a_g}{w_{00}(z_g)} \sqrt{-\frac{\lambda}{\pi \Im[1/q(z)]}}, \quad (11)$$

where a_g is the radius of the gain medium aperture, and $z_g = l_1 + f_1$ is the location of the gain medium.

B. Power Computation

As shown in Fig. 2(b), the SSLR can be equivalent to the simplest resonator which is a gain medium with two mirrors attached to each side. The resonant beam consists of two parts – the leftward-traveling wave and the rightward-traveling wave. P_1 , P_2 , P_3 , and P_4 denote the traveling wave powers at four important stages in a circulating period. The equivalent reflectivity \mathcal{R}_1 depends on the SHG efficiency η_{SHG} , the transmissivity of SHG medium Γ_{SHG} (without the SHG process), and the equivalent reflectivity of RR1 \mathcal{R}_{RR1} . The equivalent reflectivity \mathcal{R}_2 depends on the transmissivities of the gain medium Γ_g and the air Γ_{air} ; and it also depends on the equivalent reflectivity of RR2 \mathcal{R}_{RR2} and the diffraction loss coefficient Γ_{diff} . To calculate the output power of the fundamental frequency and the second-harmonic frequency released from M2, we first need to obtain the power, P_4 , of the leftward-traveling part of the resonant beam. We can calculate P_4 by solving the following equations [27]:

$$\begin{cases} P_4 = \frac{\pi a_g^2 I_s}{(1 + \sqrt{\frac{\mathcal{R}_1}{\mathcal{R}_2}})(1 - \sqrt{\mathcal{R}_2 \mathcal{R}_1})} \left[\frac{\eta_c P_{\text{in}}}{\pi a_g^2 I_s} - \ln \frac{1}{\sqrt{\mathcal{R}_2 \mathcal{R}_1}} \right], \\ \mathcal{R}_1 = (1 - \eta_{\text{SHG}})^2 \Gamma_{\text{SHG}}^2 \mathcal{R}_{\text{RR1}}, \\ \mathcal{R}_2 = \Gamma_g^2 \Gamma_{\text{air}}^2 \mathcal{R}_{\text{RR2}} \Gamma_{\text{diff}}, \\ \eta_{\text{SHG}} = \frac{8\pi^2 d_{\text{eff}}^2 l_s^2}{\varepsilon_0 c \lambda^2 n_0^3} \cdot \frac{2P_4}{\pi w^2(0)}, \end{cases} \quad (12)$$

where I_s is the saturation intensity related to the gain medium material, η_c is the combined pumping efficiency, and P_{in} is the input driving power. Note that if $P_4 < 0$, we should set $P_4 = 0$. The first line in (12) is based on the Rigrod analysis introduced in Chapter 12 in [38]. The SHG efficiency η_{SHG} depends on the resonant beam intensity at the SHG medium and the material parameters, including the efficient nonlinear coefficient d_{eff} , the crystal thickness l_s , and the refractive index n_0 ; this theory can be learned from Chapter 10 in [39]. Other factors involved in the SHG process include the resonant beam wavelength λ , the vacuum permeability ε_0 , and the speed of light c . Generally, the diffraction loss coefficient Γ_{diff} is computed using a numerical simulation program, for example, with the Fox-Li method [19]. For fast calculation, the approximation of the diffraction loss in a special case where all the devices are coaxially placed can be found in [18]. The gain medium thickness is not a factor in the calculation of the intra-cavity beam power, but it affects the absorption efficiency to the pump source which is a factor in the combined pumping

TABLE I
SYSTEM PARAMETERS

Parameter	Symbol	Value
Saturation intensity	I_s	$1.1976 \times 10^7 \text{ W/m}^2$
Resonant beam wavelength	λ	1064 nm
Combined pumping efficiency	η_c	43.9%
Efficient nonlinear coefficient	d_{eff}	4.7 pm/V
Refractive index of SHG medium	n_0	2.23
PV's responsivity	ρ	0.6 A/W
Reverse saturation current	I_0	0.32 μA
Shunt resistance	R_{sh}	53.82 Ω
Series resistance	R_s	37 m Ω
Diode ideality factor	n	1.48
Number of cells in PV panel	n_s	1
Temperature	T	298 K
PD's responsivity	γ	0.4 A/W
Load resistor at the PD	R_{IL}	10 k Ω

efficiency η_c . The rightward-traveling power outputting from the gain medium can be computed by [27]

$$P_2 = \sqrt{\frac{\mathcal{R}_1}{\mathcal{R}_2}} P_4. \quad (13)$$

The optical devices in the resonator absorb, reflect, or refract a small proportion of the passing beam, resulting in transmission loss. The air is also a loss factor in transmission, since the vapors and particles scatter/absorb the lights. As presented in [27], the received optical power from both the power transfer (PT) branch and the information transfer (IT) branch are computed as follows. The received optical power at the PV is derived from the rightward-traveling power, P_2 , outputting from the gain medium; that is

$$P_{\text{recv,PT}} = \Gamma_t^{(\nu)} P_2, \quad (14)$$

where $\Gamma_t^{(\nu)}$ is the transmission attenuation coefficient for the PT beam (at the fundamental frequency ν), namely

$$\Gamma_t^{(\nu)} = \Gamma_{\text{PV}} \Gamma_{\text{L3}} \Gamma_{\text{M3}}^{(\nu)} \Gamma_{\text{M2}}^{(\nu)} \Gamma_{\text{L2}} \Gamma_{\text{air}}, \quad (15)$$

where Γ_{PV} and Γ_{L3} are the transmissivities of the PV's incident surface and L3, respectively; and $\Gamma_{\text{M3}}^{(\nu)}$ and $\Gamma_{\text{M2}}^{(\nu)}$ are the transmissivities of M3 and M2 at frequency ν , respectively.

Similarly, as we have obtained the leftward-traveling power P_4 , the received optical power at the PD yields

$$P_{\text{recv,IT}} = 2\eta_{\text{SHG}} \Gamma_t^{(2\nu)} P_4. \quad (16)$$

Here, the transmission attenuation coefficient, $\Gamma_t^{(2\nu)}$, for the IT beam (at the second-harmonic frequency 2ν) is

$$\Gamma_t^{(2\nu)} = \Gamma_{\text{det}} \Gamma_{\text{L4}} R_{\text{M3}}^{(2\nu)} \Gamma_{\text{M2}}^{(2\nu)} \Gamma_{\text{L2}} \Gamma_{\text{air}} \Gamma_{\text{g,EOM}} \Gamma_{\text{L1}}, \quad (17)$$

where Γ_{det} , Γ_{L4} , Γ_{L2} , Γ_{L1} , and $\Gamma_{\text{g,EOM}}$ are the transmissivities of the PD's incident surface, L4, L2, L1, and the combined body of the gain medium and the EOM, respectively; $R_{\text{M3}}^{(2\nu)}$ is the reflectivity of the dichroic mirror M3 at frequency 2ν ; and $\Gamma_{\text{M2}}^{(2\nu)}$ is the transmissivity of mirror M2 at frequency 2ν .

The PT beam with optical power $P_{\text{recv,PT}}$ is received by the PV and then converted into electricity for battery charging. The charging current I_{chg} is expressed as [40, 41]

$$\begin{cases} I_{\text{chg}} = \rho P_{\text{recv,PT}} - I_d - \frac{V_d}{R_{\text{sh}}}, \\ I_d = I_0 \left[\exp\left(\frac{V_d}{n_s n V_T}\right) - 1 \right], \\ V_d = I_{\text{chg}}(R_{\text{PL}} + R_s), \\ V_T = \frac{kT}{e}, \end{cases} \quad (18)$$

where ρ is the responsivity of PV, R_{sh} is the internal equivalent shunt resistor, R_s is the internal equivalent series resistor, I_0 is the reverse saturation current, n_s is the number of cells in the PV module, n is the ideality factor of the internal equivalent diode, R_{PL} is the equivalent load resistor, k is Boltzmann's constant, T is the temperature, and e is the electron charge. The charging power, P_{chg} , which outputs from the PV also depends on the charging voltage V_{chg} on the output port. In practice, a maximum power point tracking (MPPT) circuit is connected between the PV and the battery to achieve the maximum PV conversion efficiency. In theory, employing the equivalent circuit model expressed in (18), we can obtain the charging power at the maximum power point by solving the following problem [27]:

$$\text{P1 : } P_{\text{chg}} = \max_{V_{\text{chg}}} I_{\text{chg}} V_{\text{chg}}, \quad (19)$$

$$\text{s.t. } R_{\text{PL}} = \frac{V_{\text{chg}}}{I_{\text{chg}}}, \quad (20)$$

$$0 \leq V_{\text{chg}} \leq V_{\text{oc}}, \quad (21)$$

where V_{oc} is the open-circuit voltage of the PV.

In the IT branch, the SHG beam with optical power $P_{\text{recv,IT}}$ is received at the PD. For such an intensity modulation channel, the achievable rate is obtained as [27, 42]

$$R_b = \frac{1}{2} \log_2 \left\{ 1 + \frac{(\gamma P_{\text{recv,IT}})^2}{2\pi e \sigma_n^2} \right\}, \quad (22)$$

where e is the nature constant, and σ_n^2 is the variance of the noise given by [43]

$$\sigma_n^2 = 2e(\gamma P_{\text{recv,IT}} + I_{\text{bk}})B + \frac{4kTB}{R_{\text{IL}}}, \quad (23)$$

where γ is the responsivity of the PD, $I_{\text{bk}} = 5100 \mu\text{A}$ is the background radiation-induced photon current, $B = 800 \text{ MHz}$ is the bandwidth, and $R_{\text{IL}} = 10 \text{ k}\Omega$ is the load resistance.

According to the above analysis, we find that many parameters should be optimized, including the focal lengths of the lenses, the mirror-to-lens space intervals of the FTCRs, the gain medium radius, and the reflectivity of the output mirror M2. Besides, the SHG medium thickness should be considered as a factor in the power allocation of PT and IT, as it determines the SHG efficiency. In the following section, we detail the system optimization procedure.

III. SYSTEM OPTIMIZATION

Section II has presented the system model and the system parameters which can be adjusted to optimize the system performance. Here we pursue an optimization problem to maximize the transmission efficiency defined as

$$\eta_{\text{trans}}^* = \max_{\mathbf{v}, \mathbf{m}} \frac{P_{\text{recv,PT}} + P_{\text{recv,IT}}}{P_{\text{in}}}, \quad (24)$$

where $\mathbf{v} := (l_1, f_1, l_2, f_2)$ represents the cavity structure parameter tuple that affects the resonator's stability and the TEM₀₀ mode radius; and $\mathbf{m} := (a_g, R_{\text{M2}}^{(\nu)})$ is the functional parameter tuple that affects the power loss in the power-circulating process. Here $R_{\text{M2}}^{(\nu)} = 1 - \Gamma_{\text{M2}}^{(\nu)}$ is the reflectivity of M2 at the fundamental frequency. The decision of the SHG medium thickness l_s should be considered, but it is not an optimization parameter (will be justified in Section IV). We choose l_s relying on the trade-off between PT and IT. Other parameters such as the gain medium material and thickness, the SHG medium material, and the wavelength are not the candidate parameters to be optimized, since the selection of them depends on not only the performance but also the requirements. Parameters such as I_s and η_c should be as large as possible, but these parameters depend on the selection of the material or the manufacture of the pump module.

We first optimize the cavity structure parameters to obtain a smallest TEM₀₀ mode radius at the gain medium. This optimization supports us to set the gain medium radius as small as possible, which can improve the light amplification ability of the gain medium under the same input source power. Then, two functional parameters a_g and $R_{\text{M2}}^{(\nu)}$ are optimized to reduce the power loss in the middle process of the intra-cavity power circulation. Unless otherwise specified, the parameters to be used can be found in Table I. Most parameters values are identical to those in [27], including the material parameters for the gain medium, the SHG medium, the PV and the PD. The lenses and mirrors still have absorption, reflection, or refraction at their surface even if they are coated with AR or HR coatings. Hence, we set $\{\Gamma_{\text{L1}}, \Gamma_{\text{L2}}, \Gamma_{\text{L3}}, \Gamma_{\text{L4}}, \Gamma_{\text{SHG}}, \Gamma_{\text{M2}}^{(2\nu)}, \Gamma_{\text{M3}}^{(\nu)}\} = 99\%$, $\{\Gamma_{\text{det}}, \Gamma_{\text{PV}}\} = 99.5\%$, $\{R_{\text{M1}}, R_{\text{M3}}^{(2\nu)}\} = 99.5\%$, $\Gamma_g = 98.51\%$, and $\Gamma_{\text{g,EOM}} = 97.52\%$ [27]. The loss induced by the air is distance-dependent, namely $\Gamma_{\text{air}} = e^{-\alpha d}$, where $\alpha = 0.0001$ for clear air [44].

A. Cavity Parameters

The cavity structure parameter tuple \mathbf{v} determines the resonator stability and the TEM₀₀ mode radius, $w_{00}(z_g)$, at the gain medium. The intra-cavity diffraction loss depends on the ratio of the gain medium radius to the TEM₀₀ mode radius at the gain medium, as depicted in (11). Approximately, when the gain medium radius is two or three times greater than the TEM₀₀ mode radius, the diffraction loss can be neglected. Consequently, given the expected distance d_{set} , we should find the smallest $w_{00}(z_g)$ to minimize the diffraction loss. The

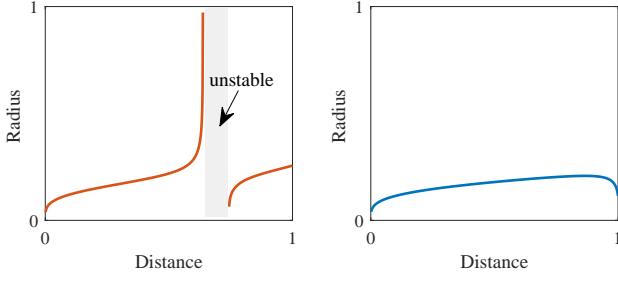


Fig. 3. Diagram of the TEM₀₀ mode radius at the gain medium varying with the transmission distance in two cases: (a) The variation is discontinuous due the existence of unstable regime; (b) the variation is continuous

optimum cavity structure parameters to provide the smallest $w_{00}(z_g)$ is obtained by solving the following problem:

$$\text{P2: } \mathbf{v}^* = \arg \min_{\mathbf{v} \in \mathbb{R}^+} w_{00}(z_g) \Big|_{d=d_{\text{set}}}, \quad (25a)$$

$$\text{s.t. } w_{00}(z_{L1}) \leq a_{L1,\text{bound}}, \quad (25b)$$

$$w_{00}(z_{L2}) \leq a_{L2,\text{bound}}, \quad (25c)$$

$$0 < g_1^* g_2^* < 1 \text{ for all } d \in [d_{\text{min}}, d_{\text{max}}]. \quad (25d)$$

The optimization search should be limited in a positive real region \mathbb{R}^+ where all the parameters are positive real numbers. The distance is set in advance to be an expected distance d_{set} . We also set the mode radius boundary at the lens L1 and L2 to be $a_{L1,\text{bound}}$ and $a_{L2,\text{bound}}$, respectively, in order to prevent any serious diffraction loss occurring at the lenses, since it will occur when the TEM₀₀ mode radius approaches or exceeds the devices' radius. As shown in Fig. 3(a), some parameters may make the cavity unstable in some distance range, which is undesired. The cavity should always be stable when the distance changes within the expected moving range $[d_{\text{min}}, d_{\text{max}}]$; see Fig. 3(b). Therefore, the condition in (25d) should be satisfied.

We solve P2 with the Monte Carlo method. The algorithm is depicted in Algorithm 1. We first choose N_s samples \mathbf{v}_i ($i = 1, 2, \dots, N_s$) randomly as the initial parameters, and find the optimum parameter tuple \mathbf{v}^* ; then, we choose a smaller search range around the optimum parameter \mathbf{v}^* , generate another series of samples randomly within the updated search range, and find the optimum one from these new samples. By repeating the above procedures, we can obtain the optimum solution. In Algorithm 1, ∞ is infinity, and $\text{rand}(\mathbf{v}_{L\text{Bound}}, \mathbf{v}_{U\text{Bound}})$ is a random function which returns a random tuple \mathbf{v} within the range lower-bounded by $\mathbf{v}_{L\text{Bound}}$ and upper-bounded by $\mathbf{v}_{U\text{Bound}}$. Note that each tuple has many elements, so in the pseudocode the statements that include tuples should be expanded independently for each element in tuples. For example, Line 22–24 should be expanded to four **if** statement blocks for f_1 , f_2 , l_1 , and l_2 independently. The input parameters $N_{\text{itr}} = 30$, $N_{\text{smax}} = 1000000$. All the elements in $\mathbf{v}_{L\text{Bound}}$ (the lower bounds for f_1 , f_2 , l_1 , and l_2) are set to zero. All the elements in $\mathbf{v}_{U\text{Bound}}$ (the upper bounds for f_1 , f_2 , l_1 , and l_2) are set to 0.006 m. $\alpha_{\text{sc}} = 0.7$ specifies a scale factor for the reduction of the search range. The remaining parameters are set as $\{d_{\text{set}}, a_{L1,\text{bound}}, a_{L2,\text{bound}}, d_{\text{min}}, d_{\text{max}}\} = \{6 \text{ m}, 3 \text{ mm}, 3 \text{ mm}, 0 \text{ m}, 6 \text{ m}\}$.

Algorithm 1 Optimizing Cavity Parameters

Input: $N_{\text{itr}}, N_{\text{smax}}, \mathbf{v}_{L\text{Bound},\text{in}}, \mathbf{v}_{U\text{Bound},\text{in}}, d_{\text{set}}, d_{\text{min}}, d_{\text{max}}, a_{L1,\text{bound}}, a_{L2,\text{bound}}, \alpha_{\text{sc}}$

Output: \mathbf{v}^*

- 1: $w_{00,\text{min}} \leftarrow +\infty$
- 2: $\mathbf{v}_{\text{diff}} \leftarrow \mathbf{v}_{U\text{Bound},\text{in}} - \mathbf{v}_{L\text{Bound},\text{in}}$
- 3: $\mathbf{v}_{L\text{Bound}} \leftarrow \mathbf{v}_{L\text{Bound},\text{in}}$
- 4: $\mathbf{v}_{U\text{Bound}} \leftarrow \mathbf{v}_{U\text{Bound},\text{in}}$
- 5: **for** $j_{\text{itr}} = 1$ to N_{itr} **do**
- 6: $N_s \leftarrow N_{\text{smax}}/j_{\text{itr}}^2$
- 7: **initializing** $\mathbf{v}[N_s]$ and \mathbf{v}^*
- 8: **for** $i = 1$ to N_s **do**
- 9: $\mathbf{v}[i] \leftarrow \text{rand}(\mathbf{v}_{L\text{Bound}}, \mathbf{v}_{U\text{Bound}})$
- 10: $w_{00,g} \leftarrow w_{00}(z_g) \Big|_{d=d_{\text{set}}, \mathbf{v}=\mathbf{v}[i]}$
- 11: **if** $w_{00,g} < w_{00,\text{min}}$
- 12: **and** $w_{00}(z_{L1}) \Big|_{d=d_{\text{set}}, \mathbf{v}=\mathbf{v}[i]} \leq a_{L1,\text{bound}}$
- 13: **and** $w_{00}(z_{L2}) \Big|_{d=d_{\text{set}}, \mathbf{v}=\mathbf{v}[i]} \leq a_{L2,\text{bound}}$
- 14: **and** $0 < g_1^* g_2^* \Big|_{\mathbf{v}=\mathbf{v}[i]} < 1$ **for** $d \in [d_{\text{min}}, d_{\text{max}}]$ **then**
- 15: $w_{00,\text{min}} \leftarrow w_{00,g}$
- 16: $\mathbf{v}^* \leftarrow \mathbf{v}[i]$
- 17: **end if**
- 18: **end for**
- 19: $\mathbf{v}_{\text{diff}} \leftarrow \alpha_{\text{sc}} \mathbf{v}_{\text{diff}}$
- 20: $\mathbf{v}_{L\text{Bound}} \leftarrow \mathbf{v}^* - \mathbf{v}_{\text{diff}}$
- 21: $\mathbf{v}_{U\text{Bound}} \leftarrow \mathbf{v}^* + \mathbf{v}_{\text{diff}}$
- 22: **if** $\mathbf{v}_{L\text{Bound}} < \mathbf{v}_{L\text{Bound},\text{in}}$ **then**
- 23: $\mathbf{v}_{L\text{Bound}} \leftarrow \mathbf{v}_{L\text{Bound},\text{in}}$
- 24: **end if**
- 25: **if** $\mathbf{v}_{U\text{Bound}} > \mathbf{v}_{U\text{Bound},\text{in}}$ **then**
- 26: $\mathbf{v}_{U\text{Bound}} \leftarrow \mathbf{v}_{U\text{Bound},\text{in}}$
- 27: **end if**
- 28: **end for**

We executed Algorithm 1 five hundred times independently. All the solutions are projected, as points, to the (f_1, f_2) plane, as shown in Fig. 4. We can observe that the solutions can be obtained almost everywhere in the (f_1, f_2) plane. The mode radius values $w_{00}(z_g)_m$ (for $m = 1, 2, 3, \dots, 500$) computed with these solutions are very close to each other, i.e., the average of these $w_{00}(z_g)_m$ values is 0.683 mm while the maximum difference among these values is 0.006 mm. This phenomenon indicates that f_1 and f_2 are not the determinants of the optimization. On the other hand, we can see that the solutions are not uniformly distributed in the (f_1, f_2) plane. Namely, large f_1 and f_2 are more possible to be found as the solution. This phenomenon is explained as follows. As depicted in (4), the equivalent focal length, f_{RR} , of the FTCCR depends on the ratio of f^2 to $(l - f)$. For larger l and f , the change of $(l - f)$ has a smaller effect on f_{RR} ; and thus, they have larger possibility to be found in the Monte Carlo method. According to the above analysis, we conclude that the selection of f_1 and f_2 only depends on the application situation. In practice, lenses with shorter focal length have more convex surface, and therefore, exhibit higher reflectivity to the edge of the incident beam. However, a very long focal length is undesired, as the FTCCR's volume will be very large.

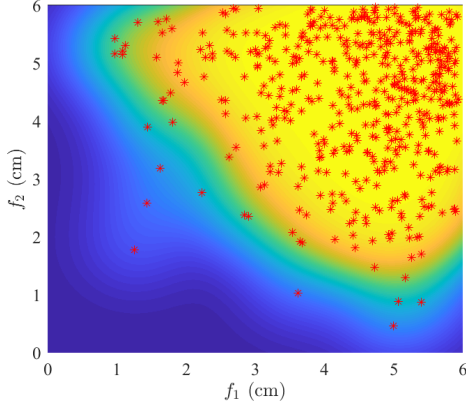


Fig. 4. Distribution of the solutions of the cavity structure parameter optimization algorithm projected on the (f_1, f_2) plane (Region with lighter color has higher probability of getting the solution)

Considering the application requirements, f_1 and f_2 should be set as the adequate values $f_{1,\text{set}}$ and $f_{2,\text{set}}$ in advance, respectively. With fixed lens focal length, we can optimize lens placement via a new optimization problem as:

$$\text{P3: } (l_1^*, l_2^*) = \arg \min_{(l_1, l_2)} w_{00}(z_g) \Big|_{\substack{d=d_{\text{set}} \\ f_1=f_{1,\text{set}} \\ f_2=f_{2,\text{set}}}}, \quad (26)$$

$$\begin{aligned} \text{s.t. } & w_{00}(z_{L1}) \leq a_{L1,\text{bound}}, \\ & w_{00}(z_{L2}) \leq a_{L2,\text{bound}}, \\ & 0 < g_1^* g_2^* < 1 \text{ for all } d \in [d_{\text{min}}, d_{\text{max}}]. \end{aligned}$$

By solving P3 with adequate preset parameters and moving range, i.e., $\{d_{\text{set}}, f_{1,\text{set}}, f_{2,\text{set}}, a_{L1,\text{bound}}, a_{L2,\text{bound}}\} = \{6 \text{ m}, 5 \text{ cm}, 5 \text{ cm}, 3 \text{ mm}, 3 \text{ mm}\}$ and $[d_{\text{min}}, d_{\text{max}}] = [0 \text{ m}, 6 \text{ m}]$, we obtain the optimum values of the mirror-to-lens intervals as

$$\begin{cases} l_1^* = 5.027 \text{ cm}, \\ l_2^* = 5.041 \text{ cm}. \end{cases} \quad (27)$$

With the optimum cavity structure parameters, we draw the curve of function $w_{00}(z)$ for $d = 1, 2, 3, \dots, 6 \text{ m}$, as depicted in Fig. 5(a). The two turning points on the left-hand side and the right-hand side of a curve represent the TEM₀₀ mode radii at lenses L1 and L2, respectively. We can observe that, at the expected transmission distance, i.e., $d = d_{\text{set}}$, the TEM₀₀ mode radius at L2, denoted by $w_{00}(z_{L2})$, reaches the given boundary. As the transmission distance d decreases, $w_{00}(z_{L2})$ decreases correspondingly. Figure 5(b) demonstrates the variation of the TEM₀₀ mode radius at the gain medium $w_{00}(z_g)$ with the distance d . We see that $w_{00}(z_g)$ reaches the maximum value of 1.09 mm at the distance of 4.32 m. Here we define a distance $d_m = 4.32 \text{ m}$ which leads to the maximum $w_{00}(z_g)$, and thus, the highest diffraction loss within the expected moving range. The following optimization is conducted under this preset distance d_m .

B. Gain Medium Aperture and SHG Medium Thickness

The next step is to optimize the gain medium radius a_g and the SHG medium thickness l_s . As mentioned before,

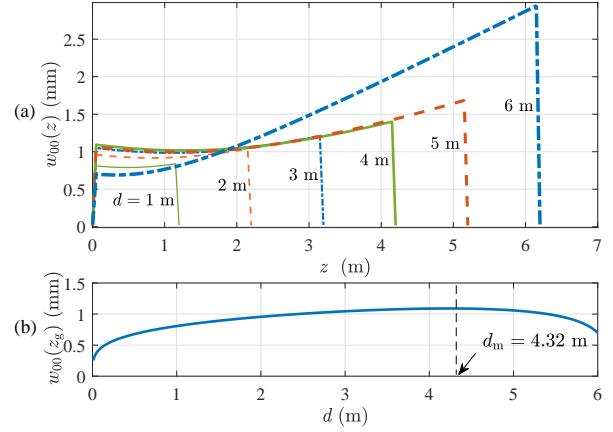


Fig. 5. TEM₀₀ mode radius w_{00} computed with the optimum cavity structure parameters obtained under $d_{\text{set}} = 6 \text{ m}$: (a) Distribution of w_{00} on the cavity axis z with different transmission distance d ; (b) w_{00} at the gain medium location z_g varies with d

reducing a_g leads to the increase of the diffraction loss. Nevertheless, increasing a_g results in the increase of the threshold power P_{th} , which also reduces the transmission efficiency η_{trans} . By reformulating (12), we obtain

$$P_4 = \eta_{\text{slop}} [P_{\text{in}} - P_{\text{th}}], \quad (28)$$

where

$$\eta_{\text{slop}} = \frac{\eta_c}{(1 + \sqrt{\frac{\mathcal{R}_1}{\mathcal{R}_2}})(1 - \sqrt{\mathcal{R}_2 \mathcal{R}_1})}, \quad (29)$$

and

$$P_{\text{th}} = \frac{\pi a_g^2 I_s}{\eta_c} \ln \frac{1}{\sqrt{\mathcal{R}_2 \mathcal{R}_1}}. \quad (30)$$

From (28–30), we observe that the threshold power P_{th} is proportional to a_g . Consequently, to balance the intra-cavity diffraction loss and the threshold power, we should find a proper a_g . Moreover, the output mirror's reflectivity $R_{M2}^{(\nu)}$ also affects the power-circulating process, as it is contained in \mathcal{R}_2 . Hence, we need to optimize a_g and $R_{M2}^{(\nu)}$ concurrently to obtain a maximum transmission efficiency. As depicted in Fig. 5(b), the TEM₀₀ mode radius at the gain medium reaches the maximum value when the receiver is at the distance d_m . Thus, the optimization is conducted under $d = d_m$. The reason is as follows. Optimizing a_g at this distance brings a minimized diffraction loss to this distance; and then, the diffraction loss will be smaller for $d \neq d_m$ due to the decreased $w_{00}(z_g)$. If the optimized a_g is obtained under other preset distance, a specific distance range around d_m will exhibit serious diffraction loss. The optimization problem is expressed as follows:

$$\text{P4: } \mathbf{m}^* = \arg \max_{\mathbf{m}} \eta_{\text{trans}} \Big|_{\substack{\mathbf{v}=\mathbf{v}^* \\ d=d_m \\ l_s=l_{s,\text{set}}}} \quad (31a)$$

$$\text{s.t. } a_g \geq w_{00}(z_g) \quad (31b)$$

$$0 \leq R_{M2}^{(\nu)} \leq 1 \quad (31c)$$

By solving P4, we can obtain the optimum functional parameter tuple $\mathbf{m}^* := (a_g^*, R_{M2}^{(\nu)*})$. Here we give an expected

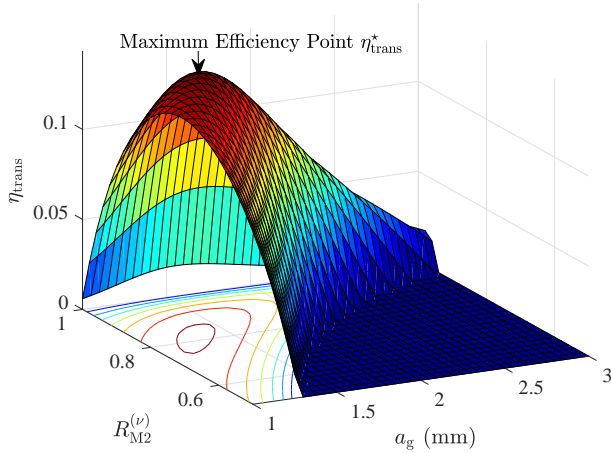


Fig. 6. Transmission efficiency η_{trans} under different reflectivity, $R_{\text{M2}}^{(\nu)}$, of the output mirror M2 and gain medium radius a_g (The driving power $P_{\text{in}}^2 = 60$ W; the SHG medium thickness $l_s = 0.5$ mm; the transmission distance $d = 4.32$ m; the focal lengths $\{f_1, f_2\} = 5$ cm; the mirror-to-lens intervals $\{l_1, l_2\}$ are obtained by optimization procedure)

SHG medium thickness $l_{s,\text{set}}$. This parameter affects the power allocation of the PT beam and the IT beam, which is discussed in the next section. As depicted in (31b), a_g is restricted to be greater than $w_{00}(z_g)$ because a smaller gain medium aperture will lead to serious diffraction loss. Besides, the reflectivity $R_{\text{M2}}^{(\nu)}$ should be in the range between 0 and 1.

The pattern of the transmission efficiency η_{trans} related to a_g and $R_{\text{M2}}^{(\nu)}$ is shown in Fig. 6. We can find that the surface has a maximum efficiency point η_{trans}^* . Therefore, P4 is a convex optimization problem. We adopt the stochastic gradient descent (SGD) algorithm to obtain a series of solutions of P4 under different l_s , as depicted in Fig. 7. We can observe that, as l_s grows, the optimum gain medium radius a_g^* and the optimum reflectivity $R_{\text{M2}}^{(\nu)*}$ increase concurrently, while η_{trans}^* decreases slowly. The change of η_{trans}^* is small. Hence, we can deem that l_s has little effect on the optimum transmission efficiency. The significant change is $R_{\text{M2}}^{(\nu)*}$ which varies from 82% to 100%, and this change correspondingly adjusts the output PT beam power. We can also observe that a_g^* changes little, especially when $l_s < 2.5$ mm. As $l_s = 4.5$ mm, the optimum reflectivity $R_{\text{M2}}^{(\nu)*}$ reaches 100%, which indicates that the charging power reduces to 0. As l_s continues to increase, $R_{\text{M2}}^{(\nu)*}$ remains at 100%, while a_g^* starts to decrease. Readers should be noticed that the SHG model is valid under the assumption that the input is a plane wave with homogeneous intensity distribution. In practice, the inhomogeneity distribution of the transverse intensity and the beam divergence may reduce the SHG efficiency; therefore, a larger l_s than the ideal case can compensate for this reduction.

We demonstrate an off-line optimization procedure, as most parameters, including the gain medium radius a_g , the reflectivity of the output mirror $R_{\text{M2}}^{(\nu)}$, and the SHG thickness l_s , can not be changed after fabrication. This procedure is important as these parameters should be determined before fabrication. An on-line optimization with respect to the lens-

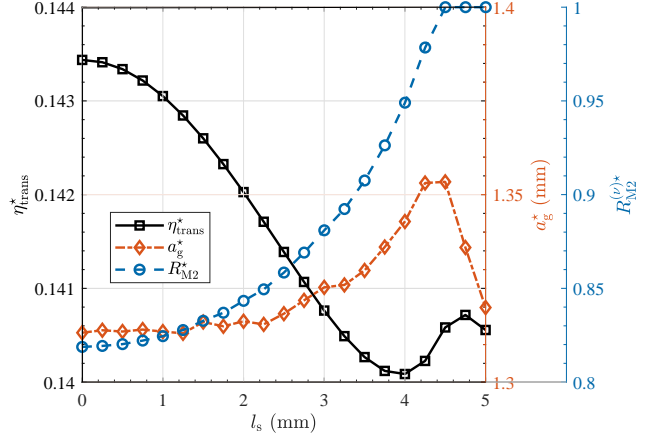


Fig. 7. The optimum transmission efficiency η_{trans}^* , gain medium radius a_g^* , output mirror reflectivity $R_{\text{M2}}^{(\nu)*}$ under different SHG medium thickness l_s (The driving power $P_{\text{in}} = 60$ W; the preset distance $d_m = 4.32$ m; the focal lengths $\{f_1, f_2\} = 5$ cm; the mirror-to-lens intervals $\{l_1, l_2\}$ are obtained by the optimization procedure)

to-mirror interval l_1 and l_2 may further improve the system performance. However, an off-line optimization is sufficient only if the application scenario is specified. For example, in a departure hall the transmitter is mounted on the ceiling, 6 m above the ground, and the receiver is taken 1 m above the ground. Assuming the FOV of the transmitter is 60° [24] and the receiver moves horizontally in the FOV, we can know that the distance between the receiver and the transmitter lies in the range of [5 m, 5.77 m]. Similarly, in a room the allowable distance lies in the range of [2 m, 2.3 m]. The distance change is small in each specific scenario. Hence, it is sufficient to choose a preset distance for each scenario.

IV. TRADE-OFF BETWEEN CHARGING POWER AND COMMUNICATION RATE

In our SWIPT system, a portion of the power is used to charge the battery at the receiver, while the other part of the power is used for information transfer. l_s affects the SHG efficiency; hence, it determines how much power is converted into the second-harmonic frequency for information carrying. In this section, we discuss the trade-off on the power allocation for wireless charging and information transfer.

All the parameters in this system affect the final charging power and achievable rate, which motivates us to investigate the following question: What is the boundary of the achievable performance? Referring to [45], we define the power-rate (P-R) region to characterize all the achievable charging power and communication rate pairs (P_{chg}, R_b) , under given input driving power P_{in} and distance d_m . By solving P4, we obtain the optimum gain medium radius a_g^* and the optimum output mirror reflectivity $R_{\text{M2}}^{(\nu)*}$. Now, we choose different SHG medium thickness ($l_s = 0, 0.25, 0.5, \dots, 4.5$ mm) and obtain the optimum parameters $(a_g^*, R_{\text{M2}}^{(\nu)*})$ for each case. Then, we use these optimum parameters to calculate the optimum charging power P_{chg}^* and the optimum rate R_b^* under

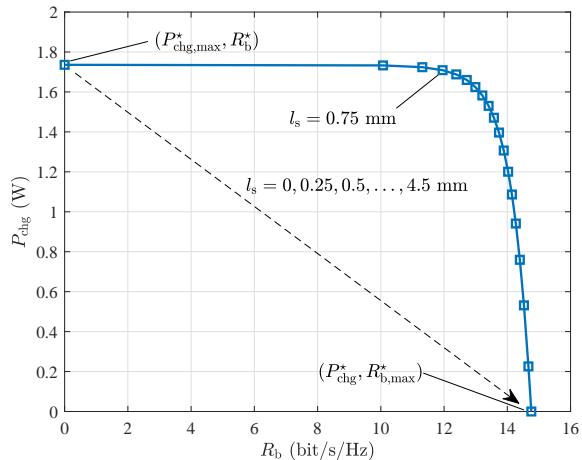


Fig. 8. Trade-off on charging power P_{chg} and achievable rate R_b (The driving power $P_{\text{in}} = 60$ W; the preset distance $d_m = 4.32$ m; the focal lengths $\{f_1, f_2\} = 5$ cm; the mirror-to-lens intervals $\{l_1, l_2\}$, the reflectivity $R_{\text{M2}}^{(\nu)}$, and the gain medium radius a_g are obtained by the optimization procedure)

distance $d = d_m$. The relation between P_{chg}^* and R_b^* is demonstrated in Fig. 8. This curve shows the boundary of the achievable (P_{chg}, R_b) pairs under this distance. The bottom-left side of the boundary is the achievable P-R region. It is easy to identify two boundary points denoted by $(P_{\text{chg,max}}^*, R_b^*)$ and $(P_{\text{chg}}^*, R_{b,max}^*)$, which show the maximum achievable charging power and communication rate, respectively. However, extremely high rate in bit/s/Hz is not useful, as the modulator accuracy is hard to support such high modulating order. On the other hand, the charging power should be as high as possible. Therefore, for practical use, the SHG medium thickness l_s can be set as 0.75 mm to obtain a very high charging power close to the maximum achievable value $P_{\text{chg,max}}^*$ while keeping the rate high enough in use.

Next, we compare the performance of the optimum design with the previous work presented in [27]. We set $P_{\text{in}} = 60$ W. Then, we solve P4 to obtain the optimum functional parameter tuple; that is $\mathbf{m}^* = (1.31 \text{ mm}, 82.2\%)$. According to the boundary of the P-C region, we decide that $l_s = 0.75$ mm. Using these optimum parameters, we calculate the charging power P_{chg} and the achievable rate R_b under different transmission distance d , as depicted in Fig. 9. As the distance is close to zero, we can see that the capacities in the two cases drop quickly. This is because the beam radius at the SHG medium becomes very large when the distance is close to zero so that the SHG efficiency is very small. We can observe that the optimized asymmetric system exhibits better performance than the non-optimized symmetric system in [27]. For 6-m distance, the charging power of the optimized system is improved by 91.8%, compared with the non-optimized symmetric system. The rate is kept above 11.3 bit/s/Hz for a large range of distance, which is also superior to the performance of the non-optimized system. Since a UAV generally needs tens-of-watts charging power, the power provided by the demonstrated system can only slightly expand the duration of flight. The achievable power

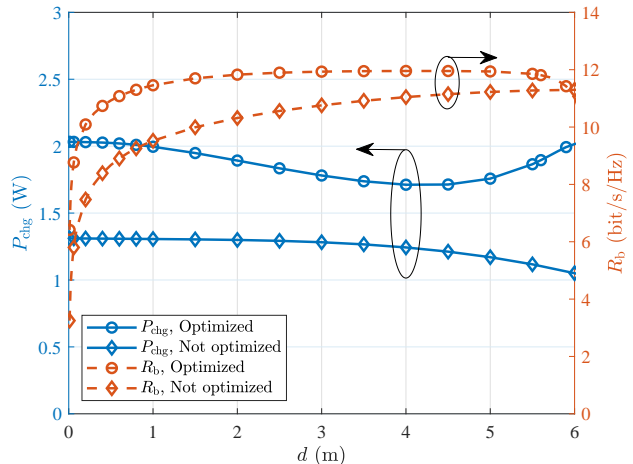


Fig. 9. Performance comparison between the optimized asymmetric system in this work and the non-optimized symmetric system in the previous work (The driving power $P_{\text{in}} = 60$ W, other parameters in this work are obtained by the presented optimization procedure)

is sufficient for portable electronic devices, such as smart watches, smart phones, electric toothbrushes. In the future, with the development of new pump modules, gain medium modules, and photovoltaic materials, the charging power has the potential to be improved, according to the analysis model. Besides, using multiple transmitters can also improve the total charging power.

V. CONCLUSIONS

In this paper, we investigated a mobile optical simultaneous wireless information and power transfer (SWIPT) system based on asymmetric spatially separated laser resonator (SSLR) and intra-cavity second harmonic generation (SHG). We created the analysis model and presented the optimization procedure for parameter determination. From the results, we found that the focal lengths of lenses in focal cat's eye retroreflectors (FTCRs) are not the crucial factors that affect the performance, but the lens-to-mirror intervals of FTCRs and some other parameters, including the gain medium radius, the reflectivity of the output mirror, and the SHG medium thickness, need to be determined by optimization algorithm. Numerical results show that the SWIPT performance in this work is greatly improved, compared with the symmetric-SSLR-based SWIPT system proposed in the previous work. Besides, we investigated the power-rate (P-R) region to demonstrate all the achievable pairs of charging power and communication rate. The boundary of the P-R region depicts the optimum performance and gives a guideline on the trade-off between power transfer and information transfer. With the trade-off strategy, the system model becomes more flexible, as it can be easily switched into a pure communication system, a pure wireless charging system, or a SWIPT system.

REFERENCES

- [1] Z. Zhang, Y. Xiao, Z. Ma, M. Xiao, Z. Ding, X. Lei, G. K. Karagiannidis, and P. Fan, "6G wireless networks: Vision,

- requirements, architecture, and key technologies,” *IEEE Veh. Technol. Mag.*, vol. 14, no. 3, pp. 28–41, Sept. 2019.
- [2] J. Yu, X. Liu, Y. Gao, and X. Shen, “3D channel tracking for uav-satellite communications in space-air-ground integrated networks,” *IEEE J. Sel. Areas Commun.*, vol. 38, no. 12, pp. 2810–2823, Dec. 2020.
 - [3] K. David and H. Berndt, “6G vision and requirements: Is there any need for beyond 5G?” *IEEE Veh. Technol. Mag.*, vol. 13, no. 3, pp. 72–80, July 2018.
 - [4] P. D. Diamantoulakis, G. K. Karagiannidis, and Z. Ding, “Simultaneous lightwave information and power transfer (SLIPT),” *IEEE Trans. Green Commun. Netw.*, vol. 2, no. 3, pp. 764–773, Sept. 2018.
 - [5] H. Asplund, D. Astely, P. von Butovitsch, T. Chapman, M. Frenne, F. Ghasemzadeh, M. Hagström, B. Hogan, G. Jöngren, J. Karlsson, F. Kronestedt, and E. Larsson, “Chapter 4 - antenna arrays and classical beamforming,” in *Advanced Antenna Systems for 5G Network Deployments*. Academic Press, 2020, pp. 89–132.
 - [6] A. M. Abdelhady, O. Amin, B. Shihada, and M.-S. Alouini, “Spectral efficiency and energy harvesting in multi-cell SLIPT systems,” *IEEE Trans. Wireless Commun.*, vol. 19, no. 5, pp. 3304–3318, May 2020.
 - [7] T. Borogovac, M. Rahaim, and J. B. Carruthers, “Spotlighting for visible light communications and illumination,” in *IEEE Globecom Workshops*, Miami, FL, USA, Dec. 2010, pp. 1077–1081.
 - [8] A. Mansour, R. Mesleh, and M. Abaza, “New challenges in wireless and free space optical communications,” *Opt. Lasers Eng.*, vol. 89, pp. 95–108, Feb. 2017.
 - [9] G. Wang, U. Habib, Z. Yan, N. J. Gomes, Q. Sui, J.-B. Wang, L. Zhang, and C. Wang, “Highly efficient optical beam steering using an in-fiber diffraction grating for full duplex indoor optical wireless communication,” *J. Lightw. Technol.*, vol. 36, no. 19, pp. 4618–4625, Oct. 2018.
 - [10] T. Koonen, A. Khalid, J. Oh, F. Gomez-Agis, and E. Tangdionga, “High-capacity optical wireless communication using 2-dimensional IR beam steering,” in *Opto-Electronics and Communications Conference (OECC) and Photonics Global Conference (PGC)*, Singapore, Nov. 2017, pp. 1–4.
 - [11] T. Koonen, J. Oh, K. Mekonnen, and E. Tangdionga, “Ultra-high capacity indoor optical wireless communication using steered pencil beams,” in *Proc. International Topical Meeting on Microwave Photonics*, Paphos, Cyprus, Oct. 2015, pp. 4802–4809.
 - [12] H. Rhee, J. You, H. Yoon, K. Han, M. Kim, B. G. Lee, S. Kim, and H. Park, “32 Gbps data transmission with 2D beam-steering using a silicon optical phased array,” *IEEE Photon. Technol. Lett.*, vol. 32, no. 13, pp. 803–806, May 2020.
 - [13] Z. Zhang, J. Dang, L. Wu, H. Wang, J. Xia, W. Lei, J. Wang, and X. You, “Optical mobile communications: Principles, implementation, and performance analysis,” *IEEE Trans. Vehi. Technol.*, vol. 68, no. 1, pp. 471–482, Nov. 2019.
 - [14] C. E. O’Lone, H. S. Dhillon, and R. Michael Buehrer, “Characterizing the first-arriving multipath component in 5G millimeter wave networks: TOA, AOA, and non-line-of-sight bias,” *IEEE Trans. Wireless Commun.*, 2021, to appear, doi:10.1109/TWC.2021.3105641.
 - [15] Q. Liu, J. Wu, P. Xia, S. Zhao, W. Chen, Y. Yang, and L. Hanzo, “Charging unplugged: Will distributed laser charging for mobile wireless power transfer work?” *IEEE Veh. Technol. Mag.*, vol. 11, no. 4, pp. 36–45, Nov. 2016.
 - [16] M. Xiong, Q. Liu, G. Wang, G. B. Giannakis, and C. Huang, “Resonant beam communications: Principles and designs,” *IEEE Commun. Mag.*, vol. 57, no. 10, pp. 34–39, Oct. 2019.
 - [17] G. J. Linford, E. R. Peressini, W. R. Sooy, and M. L. Spaeth, “Very long lasers,” *Appl. Opt.*, vol. 13, no. 2, pp. 379–390, Feb. 1974.
 - [18] M. Xiong, M. Liu, Q. Jiang, J. Zhou, Q. Liu, and H. Deng, “Retro-reflective beam communications with spatially separated laser resonator,” *IEEE Trans. Wireless Commun.*, vol. 20, no. 8, pp. 4917–4928, Aug. 2021.
 - [19] M. Liu, M. Xiong, Q. Liu, S. Zhou, and H. Deng, “Mobility-enhanced simultaneous lightwave information and power transfer,” *IEEE Trans. Wireless Commun.*, vol. 20, no. 10, pp. 6927–6939, Oct. 2021.
 - [20] W. Fang, H. Deng, Q. Liu, M. Liu, Q. Jiang, L. Yang, and G. B. Giannakis, “Safety analysis of long-range and high-power wireless power transfer using resonant beam,” *IEEE Trans. Signal Process.*, vol. 69, pp. 2833–2843, May 2021.
 - [21] Q. Liu, M. Xiong, M. Liu, Q. Jiang, W. Fang, and Y. Bai, “Charging a smartphone over the air: The resonant beam charging method,” *IEEE Internet Things J.*, 2022, to appear, DOI:10.1109/JIOT.2022.3142031.
 - [22] W. Wang, Y. Gao, D. Sun, X. Du, J. Guo, and X. Liang, “Adjustable-free and movable Nd:YVO₄ thin disk laser based on the telecentric cat’s eye cavity,” *Chin. Opt. Lett.*, vol. 19, no. 11, p. 111403, Aug. 2021.
 - [23] J. Lim, T. S. Khwaja, and J. Ha, “Wireless optical power transfer system by spatial wavelength division and distributed laser cavity resonance,” *Opt. Express*, vol. 27, no. 12, pp. A924–A935, June 2019.
 - [24] J. Liu, A. Wang, Q. Sheng, Y. Qi, S. Wang, M. Wang, D. Xu, S. Fu, W. Shi, and J. Yao, “Large-range alignment-free distributed-cavity laser based on an improved multi-lens retroreflector,” *Chin. Opt. Lett.*, vol. 20, no. 3, p. 031407, Mar. 2022.
 - [25] D. Li, Y. Tian, and C. Huang, “Capacity analysis of mobile resonant beam communications,” in *IEEE International Conference on Communications (ICC)*, Montreal, QC, Canada, June 2021.
 - [26] M. Xiong, Q. Liu, X. Wang, S. Zhou, B. Zhou, and Z. Bu, “Mobile optical communications using second harmonic of intra-cavity laser,” *IEEE Trans. Wireless Commun.*, 2021, to appear, DOI:10.1109/TWC.2021.3119412.
 - [27] M. Xiong, Q. Liu, S. Zhou, S. Han, M. Liu, and S. Zhao, “High-power and high-capacity mobile optical SWIPT,” *arXiv preprint arXiv:2107.09299*, 2021.
 - [28] N. Hodgson and H. Weber, *Laser Resonators and Beam Propagation: Fundamentals, Advanced Concepts and Applications 2nd ed.* New York, NY, U.S.: Springer, 2005.
 - [29] J. J. Snyder, “Paraxial ray analysis of a cat’s-eye retroreflector,” *Appl. Opt.*, vol. 14, no. 8, pp. 1825–1828, Aug. 1975.
 - [30] M. Liu, H. Deng, Q. Liu, J. Zhou, M. Xiong, L. Yang, and G. B. Giannakis, “Simultaneous mobile information and power transfer by resonant beam,” *IEEE Trans. Signal Process.*, vol. 69, pp. 2766–2778, May 2021.
 - [31] O. Svelto and D. C. Hanna, *Principles of lasers*. New York, NY, USA: Springer, 1998.
 - [32] X. Liu, F. Zhang, Z. Wang, N. Zong, Y. Bo, Q. Peng, D. Cui, and Z. Xu, “13 W continuous-wave intracavity frequency-doubled Nd:YAP/LBO laser at 670.8 nm,” *Opt. Rev.*, vol. 27, no. 6, pp. 493–497, Sept. 2020.
 - [33] L. Flannigan, T. Kashak, and C.-Q. Xu, “Study of fundamental wave depletion in intracavity second harmonic generation,” *Opt. Express*, vol. 29, no. 5, pp. 6810–6823, Mar. 2021.
 - [34] T. Bell and S. Ngcobo, “Intracavity second harmonic generation for higher-order laser modes,” in *Laser Resonators, Microresonators, and Beam Control XXI*, vol. 10904, San Francisco, CA, USA, Mar. 2019, pp. 175–181.
 - [35] T. D. Ponnimbaduge Perera, D. N. K. Jayakody, S. K. Sharma, S. Chatzinotas, and J. Li, “Simultaneous wireless information and power transfer (SWIPT): Recent advances and future challenges,” *IEEE Commun. Surveys Tuts.*, vol. 20, no. 1, pp. 264–302, Dec. 2018.
 - [36] H. Kogelnik, “Imaging of optical modes — resonators with internal lenses,” *Bell Syst. Tech. J.*, vol. 44, no. 3, pp. 455–494, July 1965.
 - [37] P. Baues, “Huygens’ principle in inhomogeneous, isotropic

- media and a general integral equation applicable to optical resonators,” *Opt. Quantum Electron.*, vol. 1, no. 1, pp. 37–44, Feb. 1969.
- [38] A. E. Siegman, *Lasers*. Mill Valley, CA: University Science Books, 1986.
- [39] W. Koechner, *Solid-State Laser Engineering, 6th ed.* New York, NY, USA: Springer, 2006.
- [40] J. L. Gray, *The Physics of the Solar Cell*, 2nd ed. Chichester, UK: John Wiley & Sons Ltd, 2011.
- [41] D. Sera, R. Teodorescu, and P. Rodriguez, “PV panel model based on datasheet values,” in *IEEE Int. Symposium on Industrial Electronics*, Vigo, Spain, June 2007, pp. 2392–2396.
- [42] A. Lapidoth, S. M. Moser, and M. A. Wigger, “On the capacity of free-space optical intensity channels,” *IEEE Trans. Inf. Theory*, vol. 55, no. 10, pp. 4449–4461, Oct. 2009.
- [43] A. J. C. Moreira, T. V. Rui, and A. M. de Oliveira Duarte, “Optical interference produced by artificial light,” *Wirel. Netw.*, vol. 3, no. 2, pp. 131–140, May 1997.
- [44] I. I. Kim, B. McArthur, and E. J. Korevaar, “Comparison of laser beam propagation at 785 nm and 1550 nm in fog and haze for optical wireless communications,” in *Proc. SPIE*, vol. 4214, no. 2, pp. 26–37, Feb. 2001.
- [45] R. Zhang and C. K. Ho, “MIMO broadcasting for simultaneous wireless information and power transfer,” *IEEE Trans. Wireless Commun.*, vol. 12, no. 5, pp. 1989–2001, May 2013.